Tropopause Evolution in a Rapidly Intensifying Tropical Cyclone: A Static Stability Budget Analysis

Patrick Duran* and John Molinari

University at Albany, State University of New York, Albany, NY

**Corresponding author address:* Department of Atmospheric and Environmental Sciences, University at Albany, State University of New York, 1400 Washington Avenue, Albany, NY.

E-mail: pduran2008@gmail.com

ABSTRACT

We have some cool results!

1. Introduction

After undergoing a remarkably rapid intensification (RI), Hurricane Patricia (2015) set a new record as the strongest tropical cyclone (TC) ever observed in the Western Hemisphere (Kimberlain et al. 2016; Rogers et al. 2017). High-altitude dropsonde observations taken during the Tropical Cyclone Intensity (TCI) experiment captured this RI in unprecedented detail (Doyle et al. 2017). These observations revealed remarkable changes in the structure of the cold-point tropopause and upper-level static stability as the storm intensified (Duran and Molinari 2018).

At tropical storm intensity, shortly before RI commenced, a strong inversion layer existed just above Patricia's cold-point tropopause, which was located near 17.2 km. During the first half of the RI period, this inversion layer weakened throughout Patricia's inner core, with the weakening most pronounced over the developing eye. By the time the storm reached its maximum intensity, the inversion layer over the eye had disappeared almost completely, which was accompanied by an increase in the tropopause height to a level at or above the highest-available dropsonde data point (18.3 km) at two locations. Meanwhile over the eyewall region, the static stability re-strengthened and the tropopause was limited to a level at or below 17.5 km. The mechanisms that led to these changes in upper-level static stability and tropopause height are the subject of the current paper.

Despite the importance of tropopause-layer thermodynamics in theoretical models of hurricanes (Emanuel and Rotunno 2011; Emanuel 2012), few papers have examined the upper-tropospheric evolution of TCs. Komaromi and Doyle (2017) found that stronger TCs tended to have a higher and warmer tropopause over their inner core than weaker TCs. Their results are consistent with the evolution observed over the inner core of Hurricane Patricia, in which the tropopause height increased and the tropopause temperature warmed throughout RI (Duran and Molinari 2018). The simulations of Ohno and Satoh (2015) suggested that the development of an upper-level warm core within the eye acted to decrease the static stability near the tropopause. Although the mechanisms that drive this static stability evolution have not been examined explicitly, the potential temperature (θ) budget analysis of Stern and Zhang (2013) examined the development of the TC warm core. They found that radial and vertical advection both play important roles in warm core development throughout RI, with subgrid-scale diffusion becoming particularly important during the later stage of RI.

The analysis herein is based upon that of Stern and Zhang (2013), except using a static stability budget similar to that of Kepert et al. (2016) rather than a θ budget.

2. Model Setup

The numerical simulations were performed using version 19.4 of Cloud Model 1 (CM1) described in Bryan and Rotunno (2009). The equations of motion were integrated on a 3000-km-wide, 30-km-deep axisymmetric grid with 1-km horizontal and 250-m vertical grid spacing. The computations were performed on an f-plane at 15°N latitude, over a sea surface with constant temperature of 30.5°C, which matches that observed near Hurricane Patricia (2015; Kimberlain et al. 2016). Horizontal turbulence was parameterized using the Smagorinsky scheme described in Bryan and Rotunno (2009, pg. 1773), with a prescribed mixing length that varied linearly from 100 m at a surface pressure of 1015 hPa to 1000 m at a surface pressure of 900 hPa. This formulation allows for realistically-large horizontal mixing lengths near the hurricane's inner core, consistent with the results of Bryan (2012), while not over-representing horizontal turbulence in convection at outer radii. Vertical turbulence was parameterized using the formulation of Markowski and Bryan (2016, their Eq. 6), using an asymptotic vertical mixing length of 100 m. A Rayleigh damping layer was applied outside of the 2900-km radius and above the 25-km level to prevent spurious gravity wave reflection at the model boundaries. Microphysical processes were parameterized using the Thompson et al. (2004) microphysics scheme and radiative heating tendencies were computed every two minutes using the Rapid Radiative Transfer Model for GCMs (RRTMG) longwave and shortwave schemes (Iacono et al. 2008). The initial temperature and humidity field was horizontally homogeneous and determined by averaging all Climate Forecast System Reanalysis (CFSR) grid points within 100 km of Patricia's center of circulation at 18 UTC 21 October 2015. The vortex described in Rotunno and Emanuel (1987, their Eq. 37) was used to initialize the wind field, setting all parameters equal to the values used therein.

Although hurricanes simulated in an axisymmetric framework tend to be more intense than those observed in nature, the intensity evolution of this simulation matches reasonably well with that observed in Hurricane Patricia. After an initial spin-up period of about 20 hours, the modeled storm (Fig.1, blue lines) began an RI period that lasted approximately 30 hours. After this RI, the storm continued to intensify more slowly until the maximum 10-m wind speed reached 89 m s^{-1} and the minimum sea-level pressure reached its minimum of 846 mb, 81 hours into the simulation. Hurricane Patricia (red stars) exhibited a similar intensity evolution, with an RI period leading to a maximum 10-m wind speed of 95 m s^{-1} and a minimum sea-level pressure of 872 hPa. Despite the limitations of the axisymmetric framework, the extraordinary intensity of Hurricane Patricia and the rapidity of its intensification makes Patricia a particularly good candidate for axisymmetric analysis.

3. Budget Computation

The static stability can be expressed as the squared Brunt Väisälä frequency:

$$N_m^2 = \frac{g}{T}\left(\frac{\partial T}{\partial z} + \Gamma_m\right)\left(1 + \frac{T}{R_d/R_v + q_s}\frac{\partial q_s}{\partial T}\right) - \frac{g}{1+q_t}\frac{\partial q_t}{\partial z}, \tag{1}$$

where g is gravitational acceleration, T is temperature, R_d and R_v are the gas constants of dry air and water vapor, respectively, q_s is the saturation mixing ratio, q_t is the total condensate mixing ratio, and Γ_m is the moist-adiabatic lapse rate:

$$\Gamma_m = g(1+q_t)\left(\frac{1+L_v q_s/R_d T}{c_{pm}+L_v \partial q_s/\partial T}\right), \tag{2}$$

where L_v is the latent heat of vaporization and c_{pm} is the specific heat of moist air at constant pressure. In the tropopause layer, q_s, $\partial q_s/\partial T$, and $\partial q_t/\partial z$ approach zero. In this limiting case, Eq. 1 reduces to:

$$N^2 = \frac{g}{\theta_v}\frac{\partial \theta_v}{\partial z}, \tag{3}$$

where θ_v is the virtual potential temperature. To compute N^2, CM1 uses Eq.1 in saturated environments and Eq. 3 in sub-saturated environments. For simplicity, however, only Eq. 3 will be employed for the budget computations herein[1].

Taking the time derivative of Eq. 3 yields the static stability tendency:

$$\frac{\partial N^2}{\partial t} = \frac{g}{\theta}\frac{\partial}{\partial z}\frac{\partial \theta}{\partial t} - \frac{g}{\theta^2}\frac{\partial \theta}{\partial z}\frac{\partial \theta}{\partial t}, \tag{4}$$

where the potential temperature tendency, $\partial\theta/\partial t$, can be written:

$$\frac{\partial \theta}{\partial t} = HADV + VADV + HTURB + VTURB + MP + RAD + DISS \tag{5}$$

Each term on the right-hand side of Eq. 5 represents a θ budget variable, each of which is output directly by the model every minute. HADV and VADV are the radial and vertical advective tendencies, HTURB and VTURB are the radial and vertical tendencies from the turbulence parameterization, MP is the tendency from the microphysics scheme, RAD is the tendency from the radiation scheme, and DISS is the tendency due to turbulent dissipation. This equation neglects Rayleigh damping, since this term is zero everywhere below 25 km, and the analysis domain does

[1]The validity of this approximation will be substantiated later in this section.

not extend to that level. Each term in Eq. 5 is substituted for $\partial\theta/\partial t$ in Eq. 4, yielding the contribution of each budget term to the static stability tendency. These terms are summed, yielding an instantaneous "budget change" in N^2 every minute. The budget changes are then averaged over 24-hour periods and compared to the total model change in N^2 over that same time period, i.e.:

$$\Delta N^2_{budget} = \frac{1}{\delta t}\sum_{t=t_0}^{t_0+\delta t}\frac{\partial N^2}{\partial t}\bigg|_t \tag{6}$$

$$\Delta N^2_{model} = N^2_{t_0+\delta t} - N^2_{t_0} \tag{7}$$

$$Residual = \Delta N^2_{model} - \Delta N^2_{budget} \tag{8}$$

where t_0 is an initial time and δt is 24 hours.

Eqs. 6-8 are plotted for four consecutive 24-hour periods in Fig. 2. For this and all subsequent radial-vertical cross sections, a 1-2-1 smoother is applied once in the radial direction to eliminate $2\Delta r$ noise that appears in some of the raw model output and calculated fields. The left column of Fig. 2 depicts the model changes (Eq. 7), the center column depicts the budget changes (Eq. 6), and the right column depicts the residuals (Eq. 8). In every 24-hour period, the budget changes are nearly identical to the model changes, which is reflected in the near-zero residuals in the right column. This indicates that the budget accurately represents the model variability, which implies that the neglect of moisture in the budget computation introduces negligible error within the anaysis domain[2].

In the tropopause layer, some of the budget terms are small enough to be ignored. To determine which of the budget terms are most important, a time series of the contribution of each of the budget terms in Eq. 5 to the tropopause-layer static stability tendency is plotted in Fig. 4. For this figure, each of the budget terms is computed using the method described in Section 3, except with

[2]This is not the case in the lower- and mid-troposphere, where the residual actually exceeds the budget variability in many places, likely due to the neglect of moisture; thus we limit this analysis to the upper troposphere and lower stratosphere.

1-hour averaging intervals instead of 24-hour intervals. The absolute values of these tendencies are then averaged over a radius-height domain surrounding the tropopause and plotted as a time series[3]. Advection (Fig. 4, red line) plays an important role in the mean tropopause-layer static stability tendency at all times, and vertical turbulence (Fig. 4, blue line) and radiation (Fig. 4, dark green line) also contribute significantly. Although the contribution from horizontal turbulence (Fig. 4, purple line) becomes more important after 48 hours, it is confined to a very small region immediately surrounding the eyewall tangential velocity maximum (not shown), and is negligible throughout the rest of the tropopause layer. The remaining two processes - microphysics and dissipative heating (Fig. 4, orange and light green lines, respectively) - lie atop one another near zero. These time series indicate that, at all times, three budget terms dominate the tropopause-layer static stability tendency: advection, vertical turbulence, and radiation. Variations in the magnitude and spatial structure of these terms drive the static stability changes depicted in Fig. 2; subsequent sections will focus on these variations and what causes them.

4. Results

a. Static stability evolution

The average N^2 over the first day of the simulation (Fig. 3a) indicates the presence of a weak static stability maximum just above the cold-point tropopause. This lower-stratospheric stable layer had begun to erode during the initial spin-up period, with the maximum destabilitzation occurring at the innermost radii. This decrease in static stability continued into the second day of the simulation (Fig. 3b) as the storm intensified to hurricane strength (Fig. 1). Destabilization

[3]It will be seeen in subsequent figures that each of the terms contributes both positively and negatively to the N^2 tendency within the analysis domain. Thus, taking an average over the domain tends to wash out the positive and negative contributions. To circumvent this problem, the absolute value of each of the terms is averaged.

was particularly pronounced over the developing eye, where the time-mean cold-point tropopause height increased by up to one km compared to the previous day. Over the developing eyewall and rainband regions, meanwhile, the tropopause height remained nearly constant. During the third day of the simulation (Fig. 3c), static stability over the eye continued to decrease, and the cold-point tropopause height rose to nearly 20 km over the eye. The tropopause sloped sharply downward outside of the 20-km radius, reaching a minimum altitude of 16.4 km only 45 km from the storm center. This local minimum in tropopause height corresponded to the eyewall region, where upper-tropospheric static stability increased during this time period. At larger radii, static stability began to increase in the layer immediately overlying the cold-point tropopause. This stable layer sloped upward with radius, which corresponded to an upward-sloping tropopause radially outside of the eywall region. Over the next 24 hours (Fig. 3d), as the storm's maximum 10-m wind speed remained quasi-steady near 80 m s^{-1} (Fig. 1), the tropopause-layer static stability continued to increase. Within the eye, the layer between 16 and 19 km continued to destabilize, and the cold-point tropopause height increased to a level above 21.5 km. This static stability evolution closely follows that observed in Hurricane Patricia (2015; Duran and Molinari 2018). Since most of the static stability variability

b. Static stability budget analysis

(i) 0-24 hours The first 24 hours of the simulation was characterized by a weakening of the lower-stratospheric static stability maximum above 17 km (Fig. **??**a, purple shading) and an increase in static stability below (green shading). Although these tendencies extended out to the 200-km radius, they were particularly pronounced at innermost radii. A comparison of the contributions of advection (Fig. **??**b), vertical turbulence (Fig. **??**c), and radiation (Fig. **??**d) reveals that

advection is primarily responsible for the change in static stability during this period. ...Explain this in the context of radial and vertical velocities...

(ii) 24-48 hours During the second day of the simulation, the lower-stratospheric stable layer continued to weaken (Fig. 6a). This weakening trend in the 16.75-17.75-km layer extended from the 50 km radius outward to past 200 km, and was primarily driven by advection (Fig. 6b). Below this layer, static stability began to increse slightly. This stabilization had contributions from both vertical turbulence (Fig. 6c) and radiation (Fig. 6d) in the 16-16.5-km layer. ...Explain this in context of mean vertical mixing coefficient and mean radiative heating tendency... Meanwhile, radially inward of 60 km, static stability below 17.5 km continued to weaken, primarily due to advective processes.

(iii) 48-72 hours The third day of the simulation marked a dramatic change in the structure of the tropopause-layer static stability tendencies. During this time, static stability increased markedly in an upward-sloping region within the 30-60-km radial band (Fig. 7a), and also increased within the 16.75-17.5-km layer out to at least the 200-km radius. As this layer stabilized, the layer immediately below it destabilized in a broad region extending from 60-200 km. Examination of the contribution from total advection (Fig. 7b) reveals that advection no longer dominates the static stability tendencies. Instead, a combination of vertical turbulence (Fig. 7c) and radiation (Fig. 7d) overcomes the destabilizing influence of advection to create the layer of increasing static stability. Meanwhile, the destabilizing influence of vertical turbulence in a broad region below 17 km combines with a small region of destabilization due to radiation in the 50-120-km radial band combine to destabilize the layer below 16.5 km in the 50-200-km radial band. Comparing the sum of advection and vertical turbulence (Fig. 7e) to the sum of advection, vertical turbulence,

and radiation (Fig. 7f) reveals that radiation plays a fundamental role in the re-strengthening of the lower-stratospheric stable layer during this time.

(iv) 72-96 hours

5. Discussion

Radiative heating and turbulence viscosity figures?

Discuss how turbulence increases the static stability in some regions –¿ vertical gradients of turblence intensity.

Dunion et al. speculate that the diurnal pulse only occurs in mature storms. Maybe the development of the near-tropopause stable layer could partially explain the reason for this.

Acknowledgments. We are indebted to George Bryan for his continued development and support of Cloud Model 1. We also thank Jeffrey Kepert, Robert Fovell, and Erika Navarro for helpful conversations related to this work. ADD GRANT NUMBER

References

Bryan, G. H., 2012: Effects of surface exchange coefficients and turbulence length scales on the intensity and structure of numerically simulated hurricanes. *Mon. Wea. Rev.*, **140**, 1125–1143.

Bryan, G. H., and R. Rotunno, 2009: The maximum intensity of tropical cyclones in axisymmetric numerical model simulations. *Mon. Wea. Rev.*, **137**, 1770–1789.

Doyle, J. D., and Coauthors, 2017: A view of tropical cyclones from above: The Tropical Cyclone Intensity (TCI) Experiment. *Bull. Amer. Meteor. Soc.*, **98**, 2113–2134.

Duran, P., and J. Molinari, 2018: Dramatic inner-core tropopause variability during the rapid intensification of Hurricane Patricia (2015). *Mon. Wea. Rev.*, **XXX**, XXX–XXX.

Emanuel, K., 2012: Self-stratification of tropical cyclone outflow. part ii: Implications for storm intensification. *J. Atmos. Sci.*, **69**, 988–996.

Emanuel, K., and R. Rotunno, 2011: Self-stratification of tropical cyclone outflow. part i: Implications for storm structure. *J. Atmos. Sci.*, **68**, 2236–2249.

Iacono, M. J., J. S. Delamere, E. J. Mlawer, M. W. Shephard, S. A. Clough, and W. D. Collins, 2008: Radiative forcing by long-lived greenhouse gases: Calculations with the AER radiative transfer models. *J. Geophys. Res.*, **113 (D13103)**.

Kepert, J. D., J. Schwendike, and H. Ramsay, 2016: Why is the tropical cyclone boundary layer not "well mixed"? *J. Atmos. Sci.*, **73**, 957–973.

Kimberlain, T. B., E. S. Blake, and J. P. Cangialosi, 2016: Tropical cyclone report: Hurricane Patricia. National Hurricane Center. [Available online at www.nhc.noaa.gov].

Komaromi, W. A., and J. D. Doyle, 2017: Tropical cyclone outflow and warm core structure as revealed by HS3 dropsonde data. *Mon. Wea. Rev.*, **145**, 1339–1359.

Markowski, P. M., and G. H. Bryan, 2016: LES of laminar flow in the PBL: A potential problem for convective storm simulations. *Mon. Wea. Rev.*, **144**, 1841–1850.

Ohno, T., and M. Satoh, 2015: On the warm core of a tropical cyclone formed near the tropopause. *J. Atmos. Sci.*, **72**, 551–571.

Rogers, R. F., S. Aberson, M. M. Bell, D. J. Cecil, J. D. Doyle, J. Morgerman, L. K. Shay, and C. Velden, 2017: Re-writing the tropical record books: The extraordinary intensification of Hurricane Patricia (2015). *Bull. Amer. Meteor. Soc.*, **98**, 2091–2112.

Rotunno, R., and K. A. Emanuel, 1987: An air-sea interaction theory for tropical cyclones. Part II: Evolutionary study using a nonhydrostatic axisymmetric numerical model. *J. Atmos. Sci.*, **44**, 542–561.

Stern, D. P., and F. Zhang, 2013: How does the eye warm? part i: A potential temperature budget analysis of an idealized tropical cyclone. *J. Atmos. Sci.*, **70**, 73–89.

Thompson, G., R. M. Rasmussen, and K. Manning, 2004: Explicit forecasts of winter precipitation using an improved bulk microphysics scheme. Part I: Description and sensitivity analysis. *Mon. Wea. Rev.*, **132**, 519–542.

LIST OF FIGURES

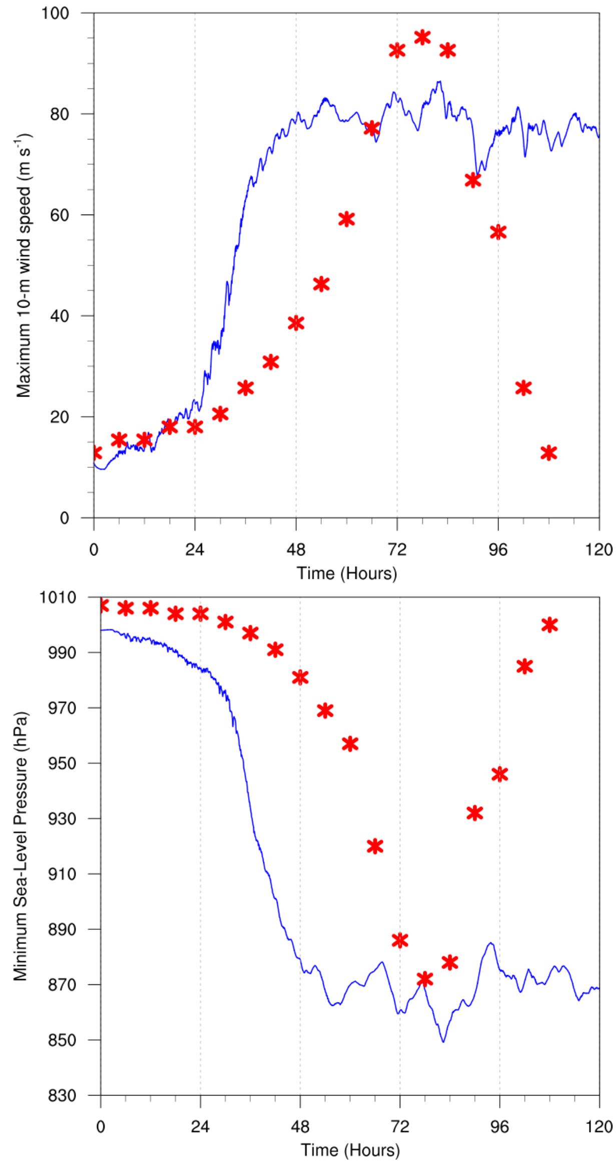

FIG. 1. The maximum 10-m wind speed (top panel; m s^{-1}) and minimum sea-level pressure (bottom panel; hPa) in the simulated storm (blue lines) and from Hurricane Patricia's best track (red stars).

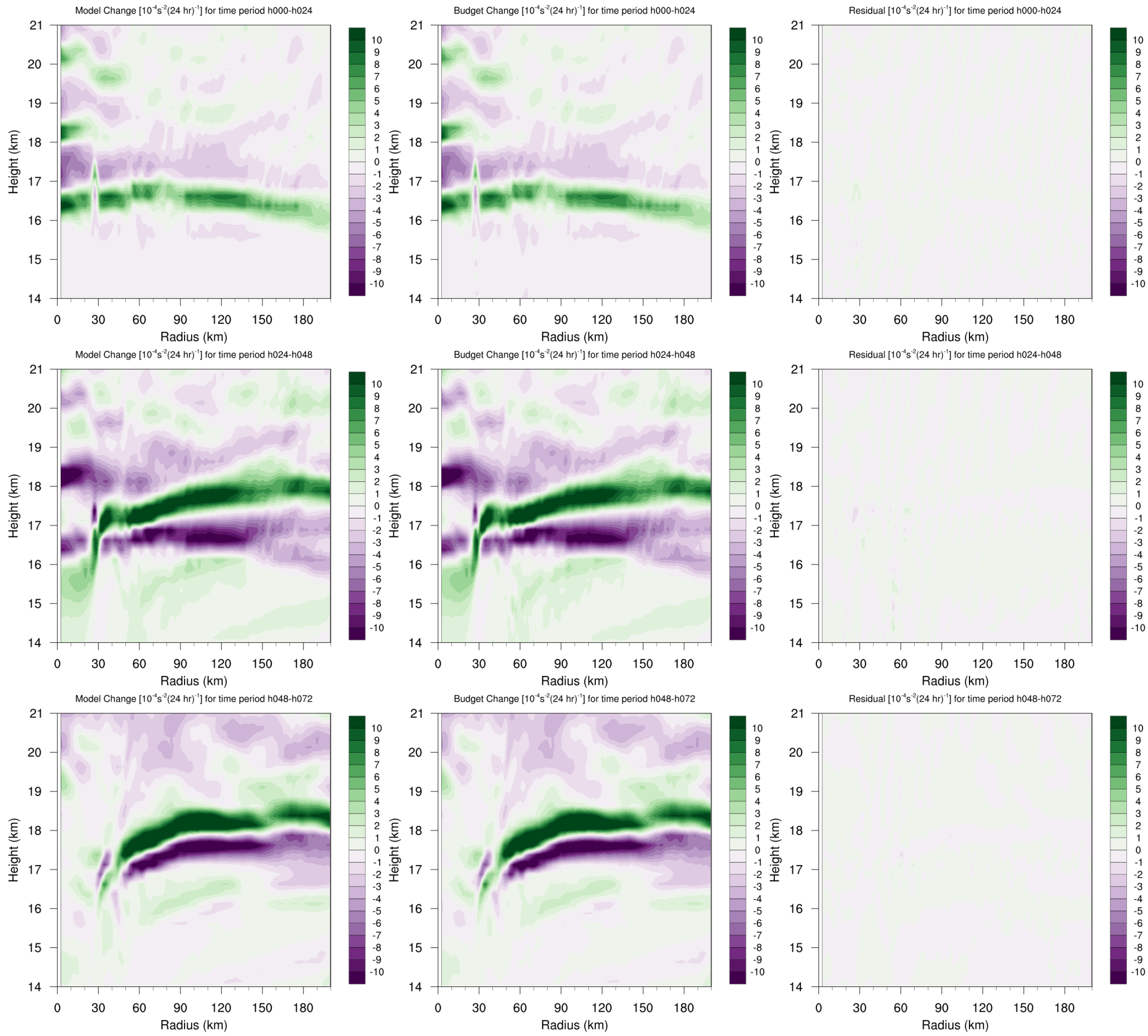

FIG. 2. Left panels: Twenty-four-hour changes in squared Brunt-Väisälä frequency (N^2; 10^{-4} s^{-2}) over (a) 0-24 hours, (b) 24-48 hours, (c) 48-72 hours, (d) 72-96 hours. Middle Panels: The N^2 change over the same time periods computed using Eq. 6. Right Panels: The budget residual over the same time periods, computed by subtracting the budget change (middle column) from the model change (left column).

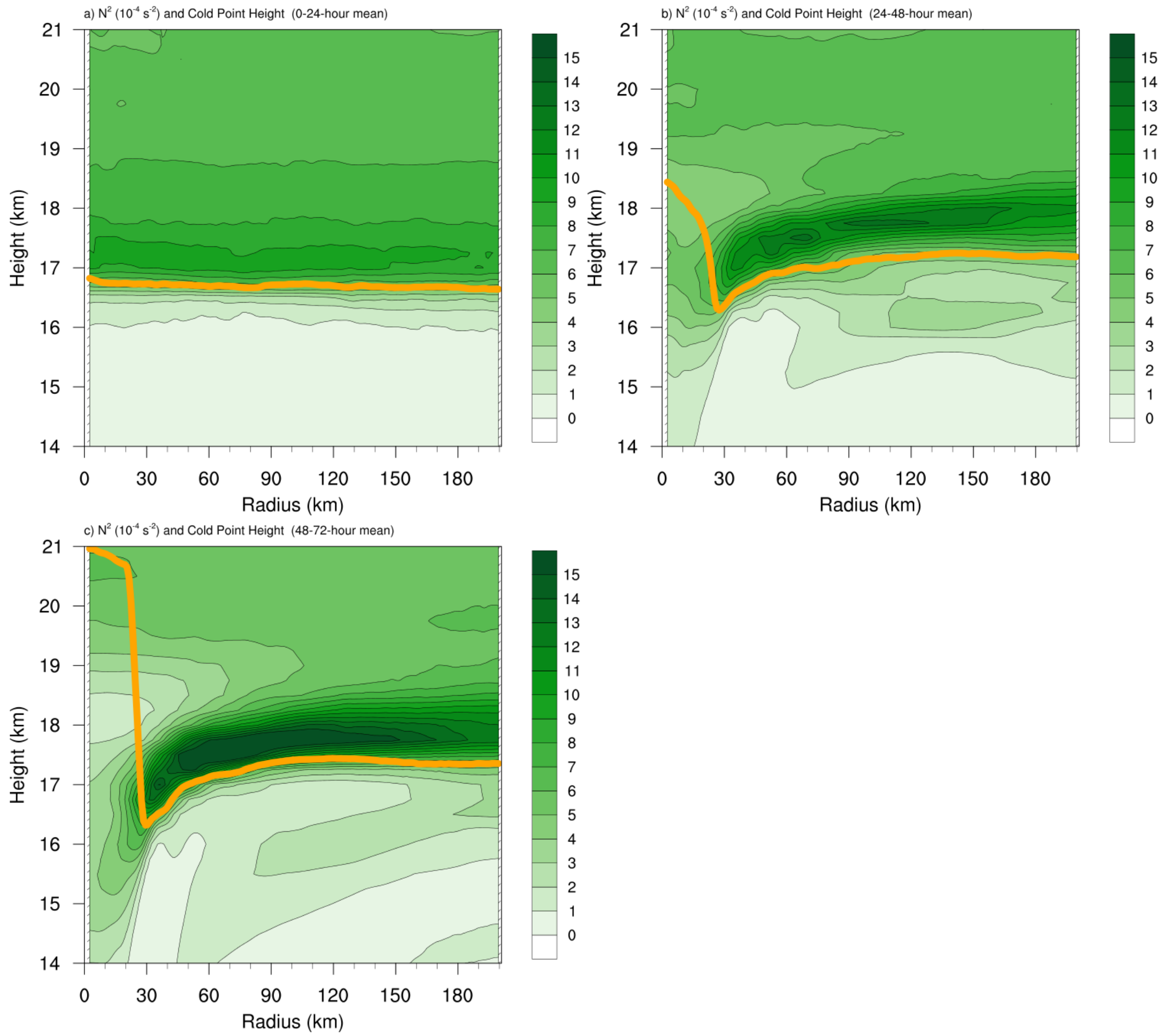

FIG. 3. Twenty-four-hour averages of squared Brunt-Väisälä frequency (10^{-4} s^{-2}) over the first four days of the simulation. Orange lines represent the cold-point tropopause determined by the mean temperature field over the same time periods.

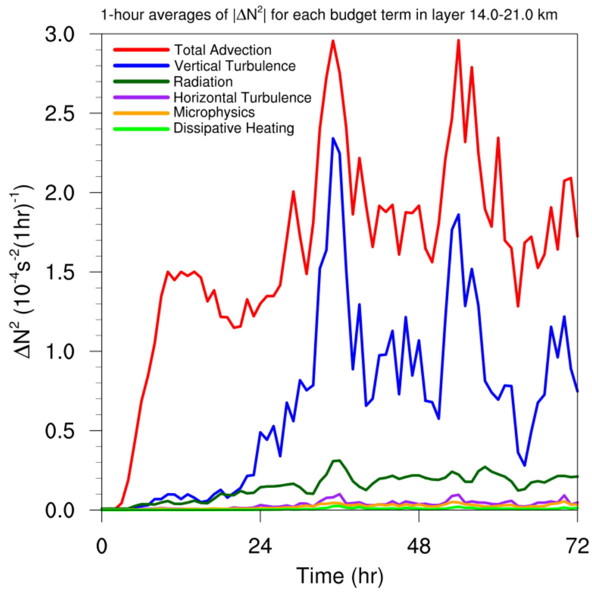

270 FIG. 4. Time series of the contribution of each of the budget terms to the time tendency of the squared
271 Brunt-Väisälä frequency (N^2; 10^{-4} s^{-2}). For each budget term, the absolute value of the N^2 tendency is averaged
272 temporally over 1-hour periods (using output every minute), and spatially in a region extending from 0 to 200
273 km radius and 14 to 21 km altitude.

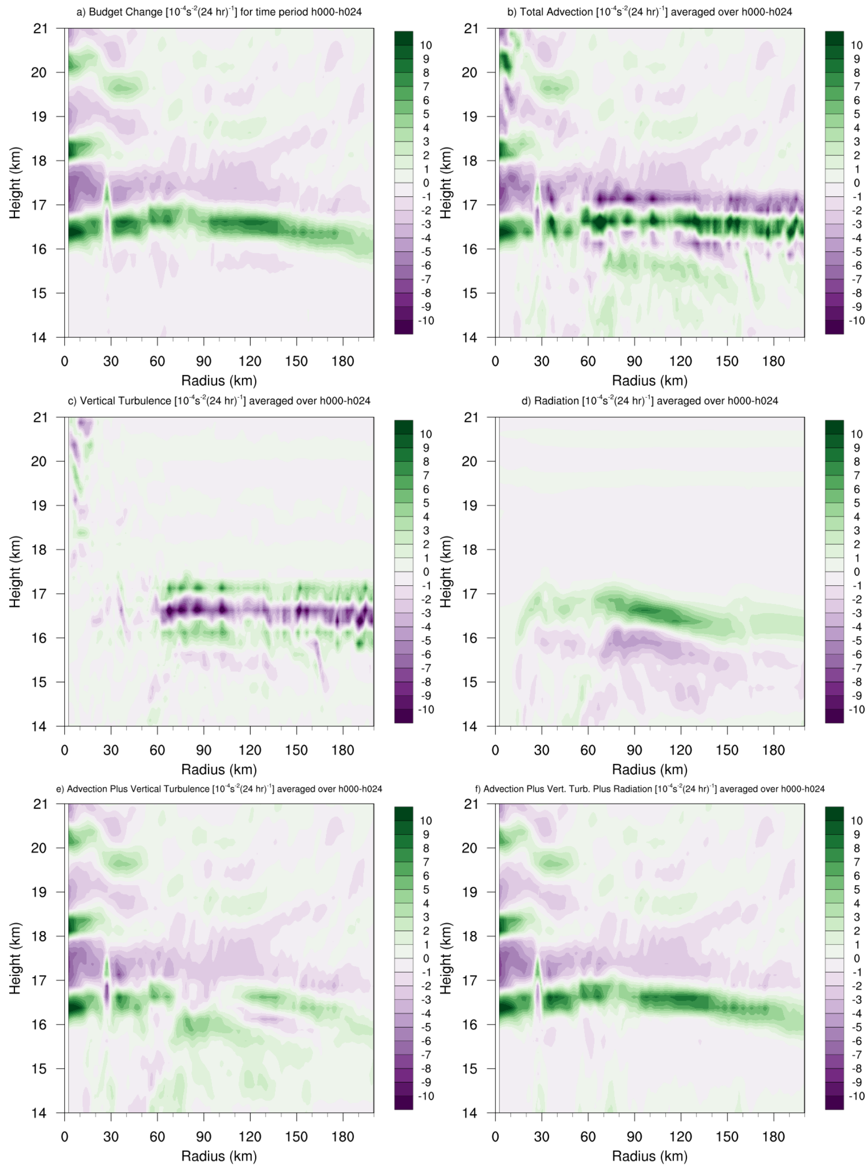

FIG. 5. (a) Total change in N^2 over the 0-24-hour period (10^{-4} s^{-2} (24 hr)$^{-1}$) and the contributions to that change from (b) the sum of horizontal and vertical advection, (c) vertical turbulence, (d) longwave and shortwave radiation, (e) the sum of horizontal advection, vertical advection, and vertical turublence, and (f) the sum of horizontal advection, vertical advection, vertical turbulence, and longwave and shortwave radiation.

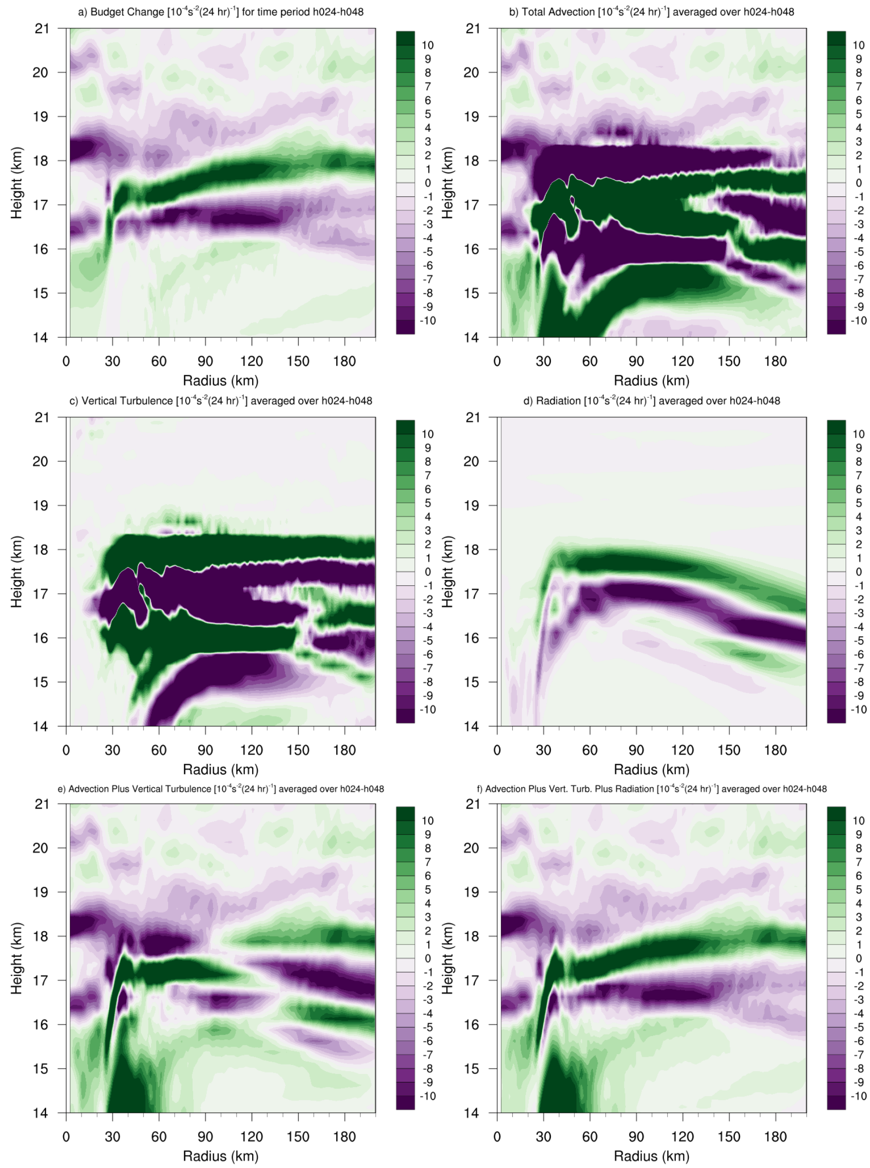

FIG. 6. As in Fig. 5, but for the 24-48-hour period.

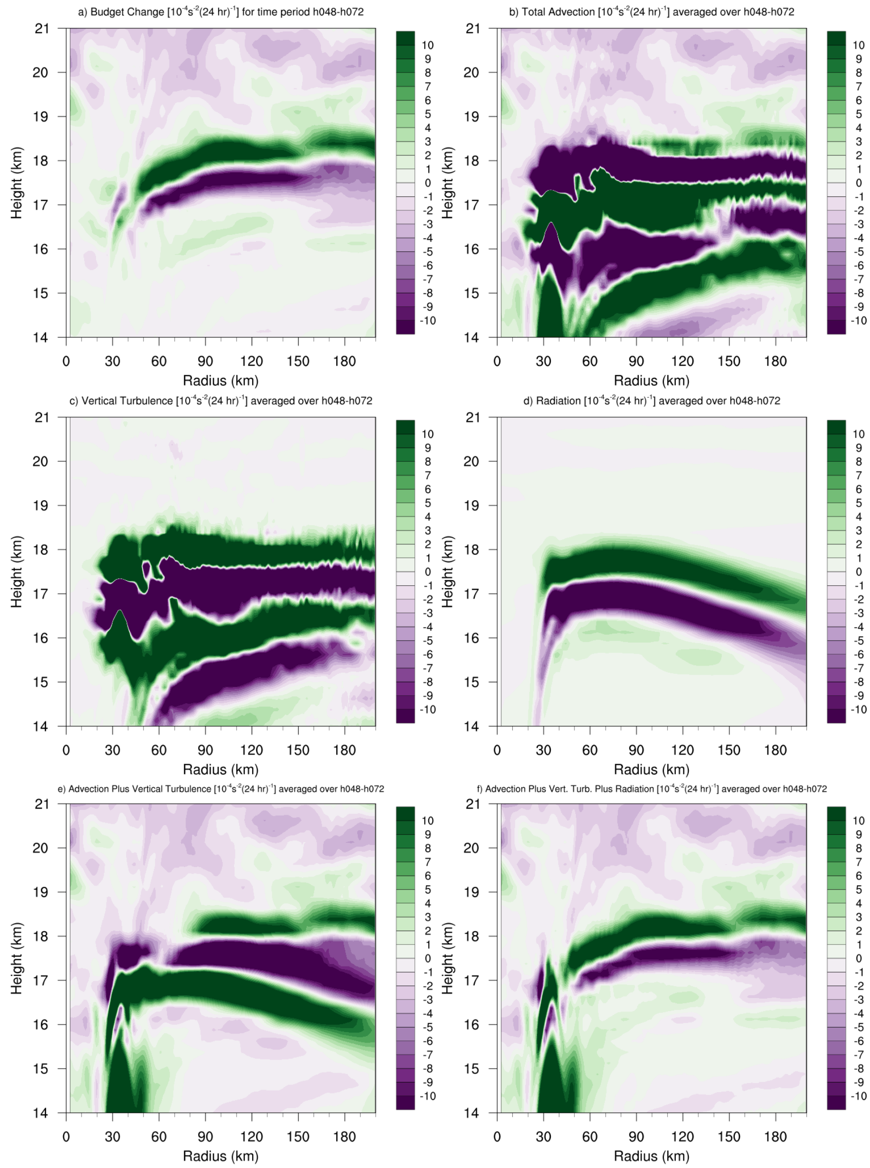

FIG. 7. As in Fig. 5, but for the 48-72-hour period.

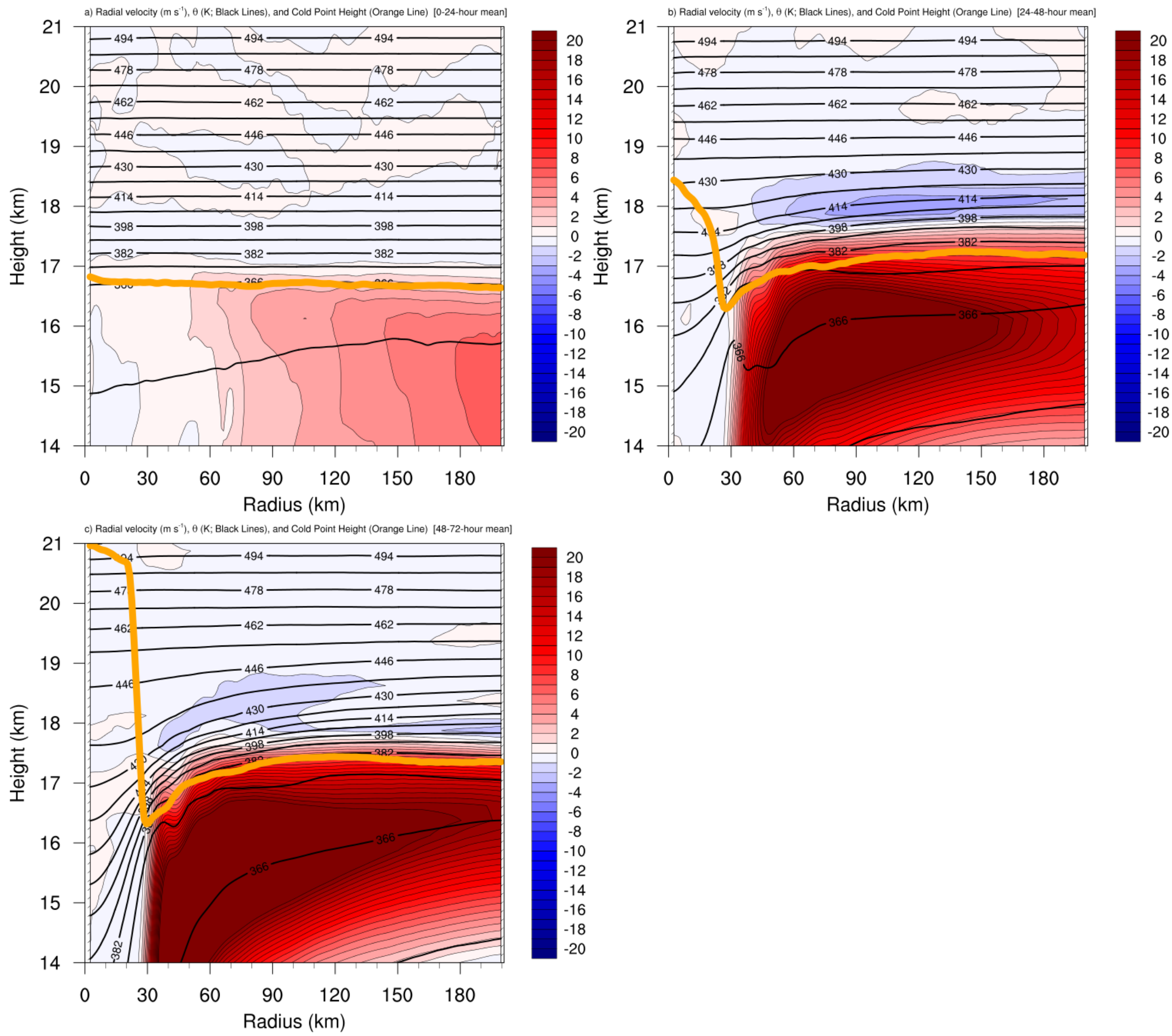

FIG. 8. Radial velocity (m s^{-1}; filled contours), potential temperature (K; thick black contours), and cold point tropopause height (orange lines) averaged over (a) 0-24 hours, (b) 24-48 hours, and (c) 48-72 hours.

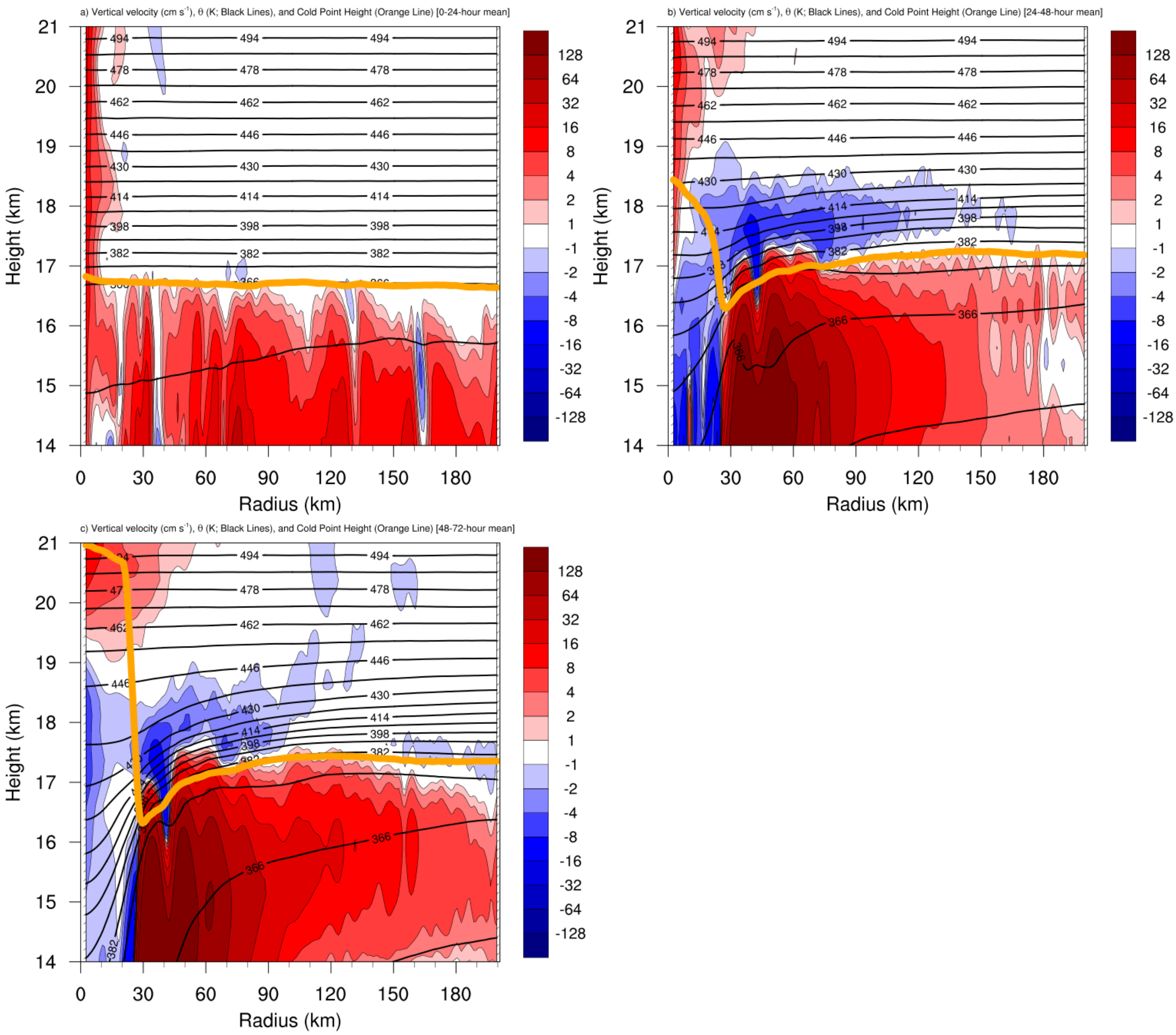

FIG. 9. Vertical velocity (cm s^{-1}; filled contours), potential temperature (K; thick black contours), and cold point tropopause height (orange lines) averaged over (a) 0-24 hours, (b) 24-48 hours, and (c) 48-72 hours.

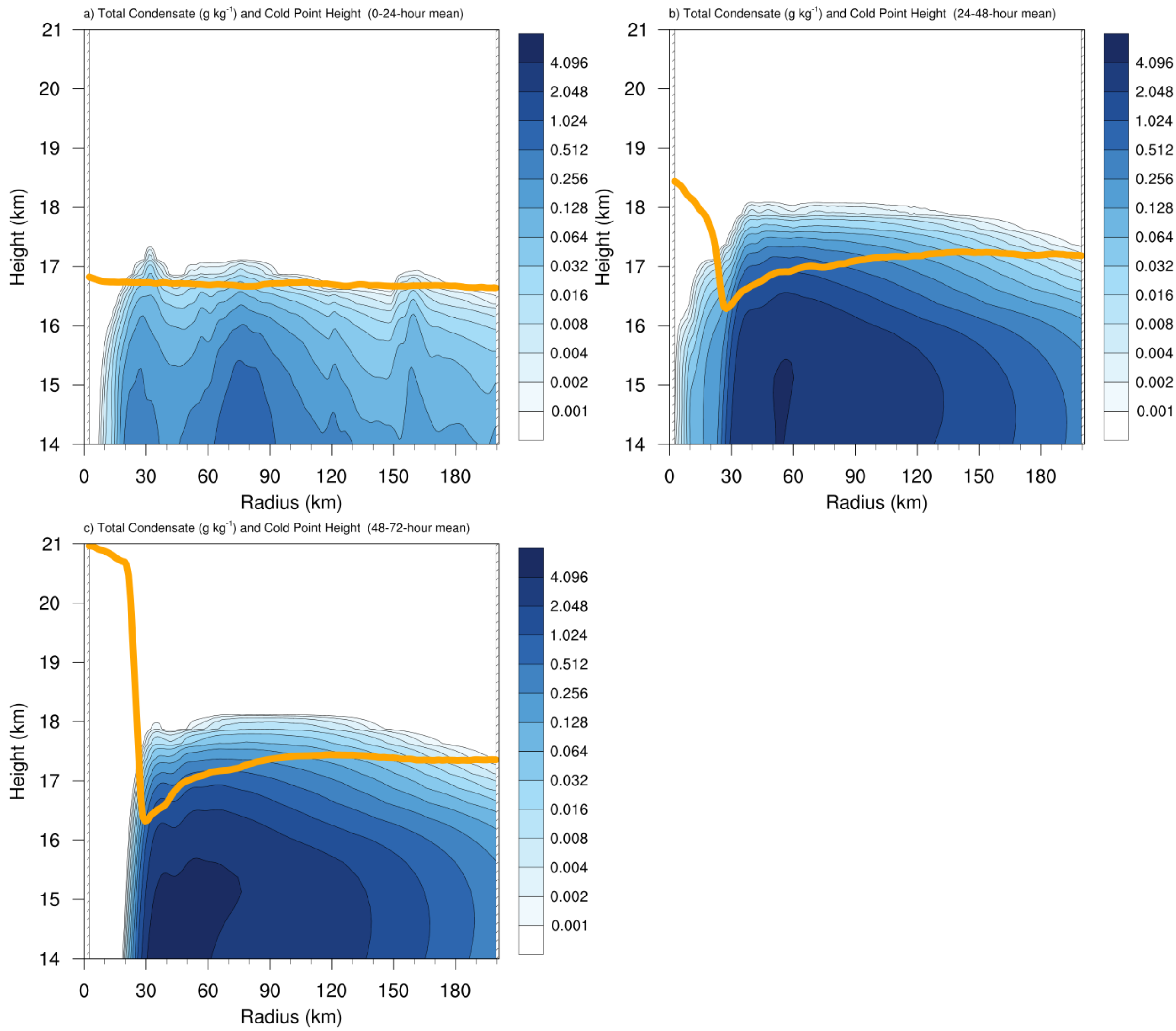

FIG. 10. Total condensate mixing ratio (g kg^{-1}) and cold point tropopause height (orange lines) averaged over (a) 0-24 hours, (b) 24-48 hours, and (c) 48-72 hours.

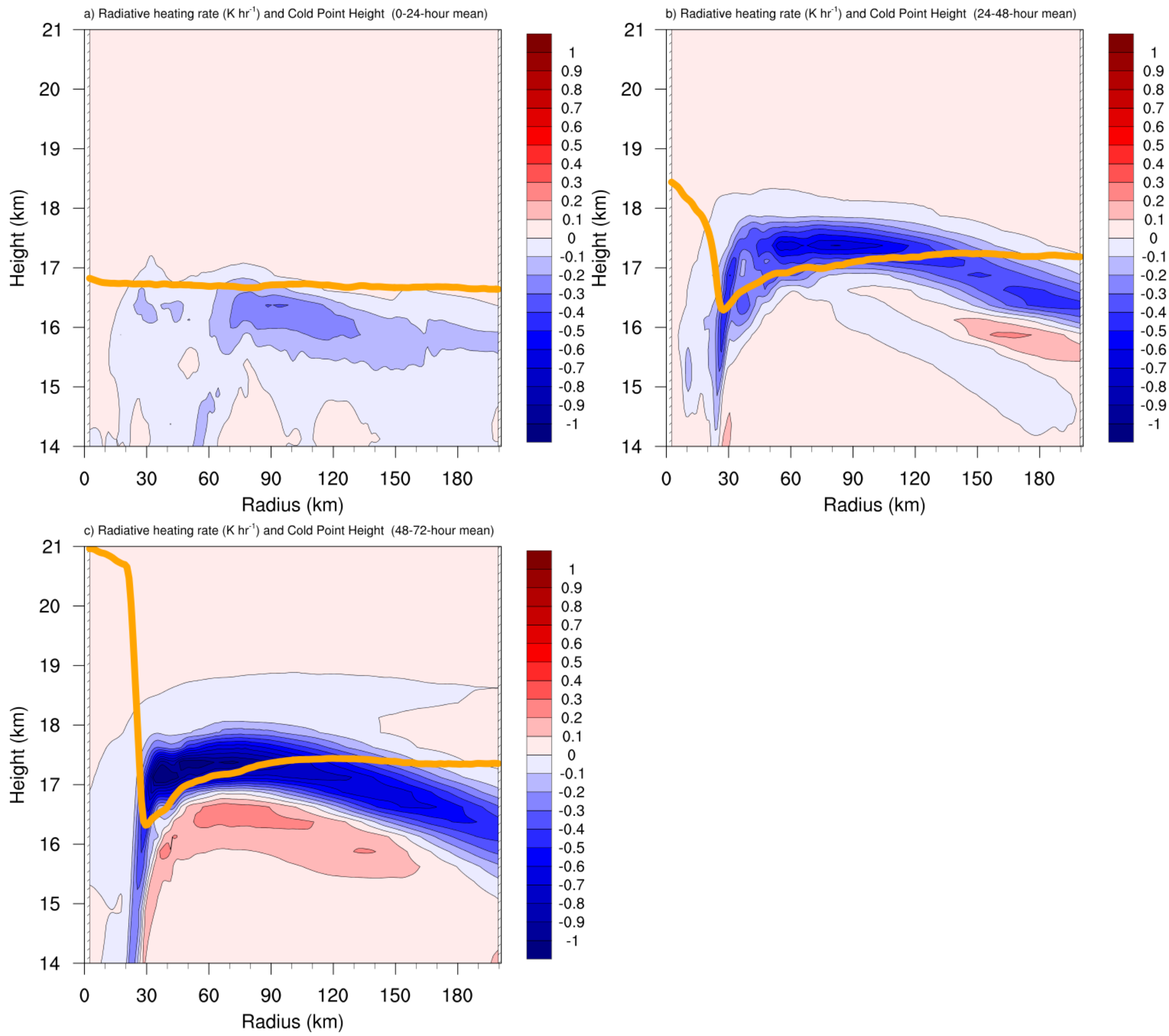

FIG. 11. Radiative heating rate (K hr^{-1}) and cold point tropopause height (orange lines) averaged over (a) 0-24 hours, (b) 24-48 hours, and (c) 48-72 hours.

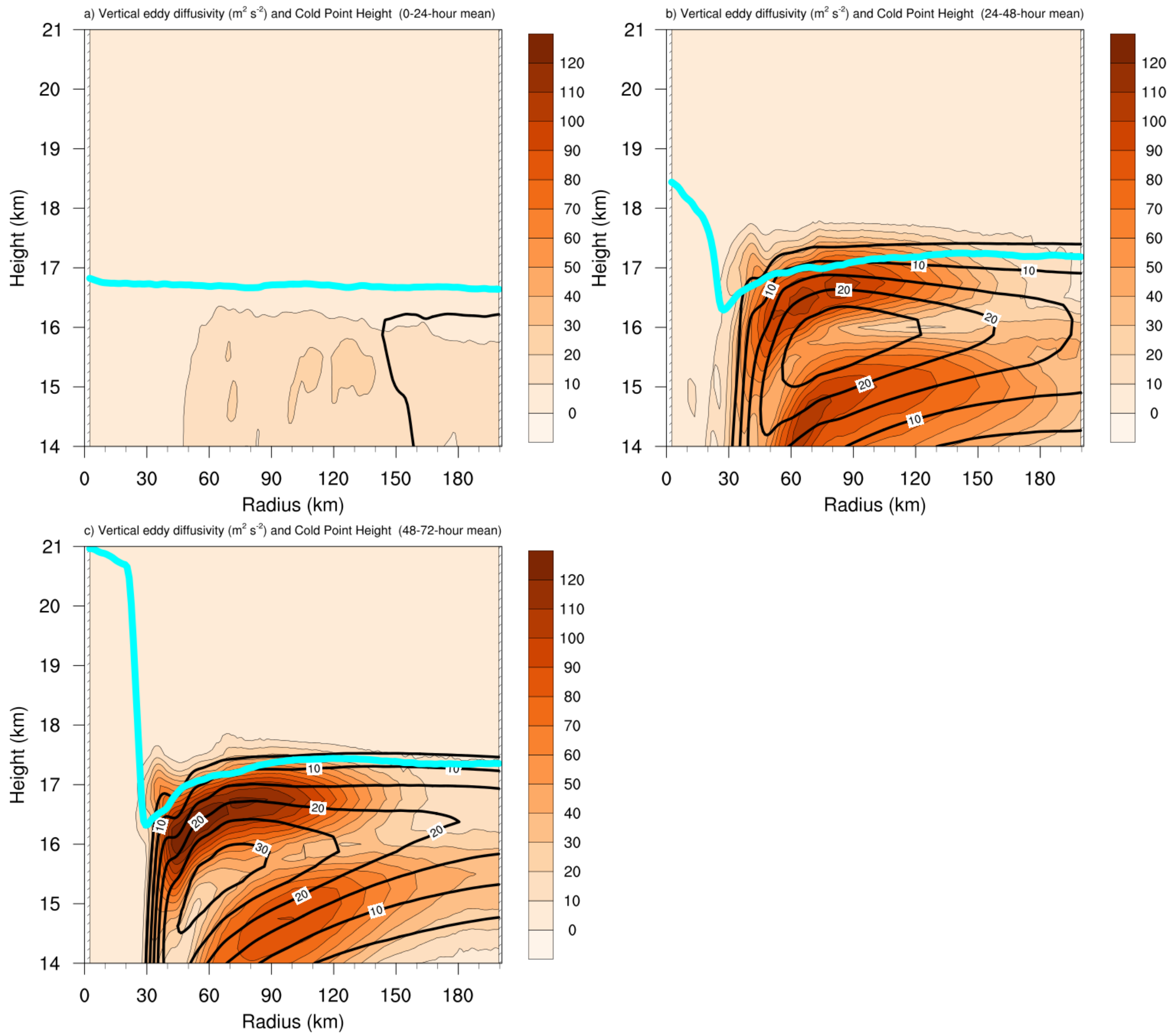

FIG. 12. Vertical eddy diffusivity (m^2 s^{-2}; filled contours), cold point tropopause height (cyan lines), and radial velocity (m s^{-1}; thick black lines) averaged over (a) 0-24 hours, (b) 24-48 hours, and (c) 48-72 hours.